PAPER

Magnetic iron oxide and iron oxide@gold nanoparticle anchored nitrogen and sulfur-functionalized reduced graphene oxide electrocatalyst for methanol oxidation

Necip Atar,*[a] Tanju Eren,[a] Mehmet Lütfi Yola,[b] Hassan Karimi-Maleh*[c] and Bermali Demirdögen[a]

Fuel cells have been attracting more and more attention in recent decades due to high-energy demands, fossil fuel depletions and environmental pollution throughout world. In this study, we report the synthesis of metallic and bimetallic nanoparticles such as spherical iron oxide nanoparticles [(sp)Fe_3O_4], rod iron oxide nanoparticles [(rd)Fe_3O_4] and iron@gold nanoparticles (Fe_3O_4@AuNPs) involving L-cysteine functionalized reduced graphene oxide nanohybrids [(sp)Fe_3O_4/cys/rGO, (rd)Fe_3O_4/cys/rGO and Fe_3O_4@AuNPs/cys/rGO] and their application as an electrocatalyst for methanol electro-oxidation. The nanohybrids have been characterized by transmission electron microscopy (TEM), X-ray photoelectron spectroscopy (XPS) and X-ray diffraction (XRD). The experimental results have demonstrated that reduced graphene oxide-supported bimetallic nanoparticles enhanced the electrochemical efficiency for methanol electro-oxidation with regard to diffusion efficiency, oxidation potential and forward oxidation peak current. Fe_3O_4@AuNPs/cys/rGO, in comparison to (sp)Fe_3O_4/cys/rGO and (rd)Fe_3O_4/cys/rGO, showed the most efficiency for methanol electro-oxidation.

1. Introduction

Fuel cells are electrochemical cells used to generate electricity from fuels, and recently have drawn more attention as an alternative method for energy production.[1,2] One example of these cells is direct methanol fuel cells (DMFCs) which are used for operating portable electronic devices.[3,4] Methanol is preferred because it has some significant advantages in supply, transport, and storage.[5,6] More importantly methanol's energy density is higher than gaseous hydrogen, and can integrate into the existing energy infrastructure.[7,8] Many research groups have investigated the electro-oxidation of methanol in direct methanol fuel cells.[3,4,9,10] Although Pt and Pt-based alloys (with metals such as Ru, Pd, Au, Ni *etc.*) are the most promising anode catalysts in DMFCs, high cost and limited supply of Pt put some restrictions on large-scale applications.[1] Recently, bimetallic nanoparticles (NPs) have been employed as catalysts in nanotechnology researches.[11–15] Bimetallic NPs generally show better catalytic properties than their monometallic forms.[11,15] Use of NPs has some certain advantages.[16–21] First, bimetallic

nanoparticles consist of two different metals which are combined, and this can create a synergetic effect in specific properties such as size dependent optic, electronic and catalytic properties. Secondly, use of bimetallic nanoparticles allows reducing the amount of expensive catalyst, since a less expensive metal can be employed as the core material.[11,12] Moreover, because surface area is larger and the majority of atoms can be used at nanoscale, NPs can increase reaction rate and selectivity.[1,11,22] Studies showed that the catalytic activity of NPs is determined by some parameters including shape, structure, composition and architecture.[23–27] Over the last decade, additional control and design of magnetic nanoparticles were achieved by developing core–shell structured nanomaterials like Fe_3O_4@AuNPs that we studied in this paper. The core properties of these particles have providing an increased number of catalytic applications. In the structure of gold-coated Fe_3O_4@AuNPs core–shell nanoparticles, the magnetic Fe_3O_4 nanoparticles are important about enhancing the chemical stability by protecting the core from corrosion and displaying fine compatibility and affinity. The significantly enhanced electrocatalytic performance of Fe_3O_4@AuNPs core–shell nanoparticles can be attributed to the large surface area resulting from the formation of the bimetallic nanoparticle on rGO sheets and also the improved conductivity.[12] We studied the bimetallic magnetic core–shell Fe_3O_4@AuNPs with composing rGO to improve the surface properties and support the catalysis of methanol oxidation.

[a]*Department of Chemical Engineering, Pamukkale University, Denizli, Turkey. E-mail: necipatar@gmail.com; h.karimi.maleh@gmail.com; Tel: +98-911-254-0112*

[b]*Department of Metallurgical and Materials Engineering, Sinop University, Sinop, Turkey*

[c]*Department of Chemistry, Graduate University of Advanced Technology, Kerman, Iran*

Graphene has become interesting for scientist from different fields because of its high elasticity, thermal conductivity, surface area and mechanical strength, and used as catalyst support in fuel cells.[1] Graphene has a two dimensional structure in which carbon atoms forms a honeycomb-like structure *via* sp^2 hybridization, and carbon is the only one-atom-thick material.[24,28] Graphene shows exceptional properties due to this hexagonal structure and electron configuration. Graphene oxide (GO) is the oxidation product of graphene and like graphene it has a two-dimensional (2D) crystal structure. GO shows different chemical and physical properties than graphene.[28,29] In some cases it necessary to regain graphene's desirable properties such as electrical conductivity. For this purpose GO is generally reduced by thermal annealing or chemical reducing agents forming reduced graphene oxide (r-GO).[30,31]

The aim of this study is to synthesize metallic and bimetallic nanoparticles and functionalized reduced graphene oxide containing nanohybrid [(sp)Fe_3O_4/cys/rGO, (rd)Fe_3O_4/cys/rGO and Fe_3O_4@AuNPs/cys/rGO] catalysts for methanol electro-oxidation applications.

2. Experimental

2.1. Materials

All chemicals that used in the experiments were reagent grade and were used as received following; graphite powder (Merck, Germany), sulfuric acid (H_2SO_4, Merck, Germany), potassium persulfate ($K_2S_2O_8$, Merck, Germany), phosphorus pentoxide (P_2O_5, Merck, Germany), potassium permanganate ($KMnO_4$, Merck, Germany), hydrogen peroxide (H_2O_2, Merck, Germany), ethanol (Merck, Germany), hydrochloric acid (HCl, Sigma-Aldrich), *N*-(3-dimethylaminopropyl)-*N*′-ethyl-carbodiimidehydrochloride (EDC, Sigma-Aldrich, USA), ethanol (Sigma-Aldrich, USA), β-cyclodextrin (Sigma-Aldrich, USA), L-cysteine (cys, Sigma-Aldrich, USA), $HAuCl_4$ (Sigma-Aldrich, USA), sodium citrate (Merck, Germany), isopropyl alcohol (IPA, Sigma-Aldrich, USA), methanol (Merck, Germany), HPLC grade acetonitrile (MeCN, Sigma-Aldrich, USA), $NaBH_4$ (Merck, Germany), perchloric acid ($HClO_4$, Sigma-Aldrich, USA), hydrazine hydrate (Merck, Germany) and other chemicals were reagent grade quality and were used as received. The ultra-pure water with resistance of 18.3 MΩ cm (Human Power 1$^+$ Scholar purification system) was used in the experiments of aqueous media.

2.2. Instrumentation

All electrochemical experiments were performed using a BAS-100B electrochemical analyzer (Bioanalytical System Inc., Lafayette, IL, U.S.) and Gamry Reference 600 work-station. Argon gas was passed through the solutions during experiments for about 10 min.

JEOL 2100 HRTEM (JEOL Ltd., Tokyo, Japan) and ZEISS EVO 50 SEM (GERMANY) analytic microscopies were used to investigate the morphologies of (sp)Fe_3O_4/cys/rGO, (rd)Fe_3O_4/cys/rGO and Fe_3O_4@AuNPs/cys/rGO nanocomposites.

XPS analysis were performed on a PHI 5000 Versa Probe (Φ ULVAC-PHI, Inc., Japan/USA) model with monochromatized Al Kα radiation (1486.6 eV) as an X-ray anode operated at 50 W. To prepare the samples, one drop of the prepared (sp)Fe_3O_4/cys/rGO, (rd)Fe_3O_4/cys/rGO and Fe_3O_4@AuNPs/cys/rGO solutions were placed on clear glass and then dried in air.

A Rigaku Miniflex X-ray diffractometer was used for X-ray diffraction measurements of the (sp)Fe_3O_4/cys/rGO, (rd)Fe_3O_4/cys/rGO and Fe_3O_4@AuNPs/cys/rGO composites nanostructures. A scanning speed of $2\theta = 2°$ min^{-1} with a step size of $0.02°$ was used to examine the samples.

2.3. Synthesis of rGO

GO was prepared by the modified Hummers method.[12] Typically, 2.5 g of graphite powder were placed in a flask containing a mixture of 12.5 mL of H_2SO_4 (98%), 2.5 g of $K_2S_2O_8$ and 2.5 g of P_2O_5. The mixture was kept at 80 °C for 6 h. Then, the mixture was cooled to room temperature and added with 500 mL of ultra-pure water. The product was filtered and washed with ultra-pure water and 125 mL of H_2SO_4 (98%) was added at 0 °C. Later, 15 g of $KMnO_4$ were added to the stirring suspension which was kept at 20 °C. After the feeding of $KMnO_4$ was finished, the flask was heated to 50 °C. After 4 h, 500 mL of ultra-pure water were added to the mixture in an ice bath. The last mixture was stirred for 2 h and diluted to 1 L with ultra-pure water. After that, the suspension was fed slowly with 20 mL of H_2O_2 (30%) and the solution started bubbling. The color of the suspension changed to brilliant yellow from brownish. The synthesized graphite oxide was filtered and washed with 0.1 M HCl and ultra-pure water three times. The graphite oxide was collected by an ultracentrifuge.

The as-prepared GO was dispersed into 200 mL water under mild ultrasound yielding a yellow-brown suspension, then 4 mL hydrazine hydrate (80 wt%) were added and the solution was heated in an oil bath maintaining at 100 °C under a water-cooled condenser for 24 h. After the reaction, the prepared rGO product was collected by vacuum filtration.

2.4. Synthesis of (sp)Fe_3O_4, (rd)Fe_3O_4 and Fe_3O_4@AuNPs

The (sp)Fe_3O_4 were synthesized in aqueous solution without any surfactants.[32] In this method, ferric and ferrous ions are mixed in highly basic solution at room temperature. $FeCl_3$ (0.0125 M, 97%) and $FeCl_2$ (0.0125 M, 98%), were mixed with 25 mL of ultra-pure water. Then, 20 mL of NH_3 (28%) was added to the mixture and the resulting solutions were stirred for about 10 min. Here in, black precipitates were immediately formed, which were filtrated and washed with ultra-pure water for several times to remove impurities. Lastly, the precipitates were dried in furnace at 80 °C for 6 h. To synthesis the rod shaped Fe nanoparticles, first of all, 2 mmol of $FeCl_3 \cdot 6H_2O$ and 20 mmol of NaOH were mixed with 20 mL of ultra-pure water and 6 mmol of 1-butyl-3-methylimidazolium chloride were added drop by drop during mixing until a homogenous solution were formed. After 20 min of mixing procedure, the mixture was kept in an autoclave with a heat of 150 °C for 6 hours. After the reaction complete, the mixture was cooled at room temperature. After

that the mixture was filtrated and washed with ultra-pure water and ethanol. Finally the mixture was heated to 380–400 °C until a dark red (rd)Fe$_3$O$_4$ solution was formed. For preparation Fe$_3$O$_4$@AuNPs, Fe(NO$_3$)$_3$ (4 mL, 0.01 M) was reduced by 0.1 M ascorbic acid (20 mL) for 20 min at room temperature under a nitrogen atmosphere. The pH of the solution was adjusted to 4.0 and the HAuCl$_4$ (4 mL, 0.01 M) was added at room temperature for 1 h. A dark solid indicated that the iron oxide core was coated with a gold shell. Then, the product was separated by a magnet and washed with water. The Fe$_3$O$_4$@AuNPs was dried overnight in a vacuum oven at 25 °C.[14]
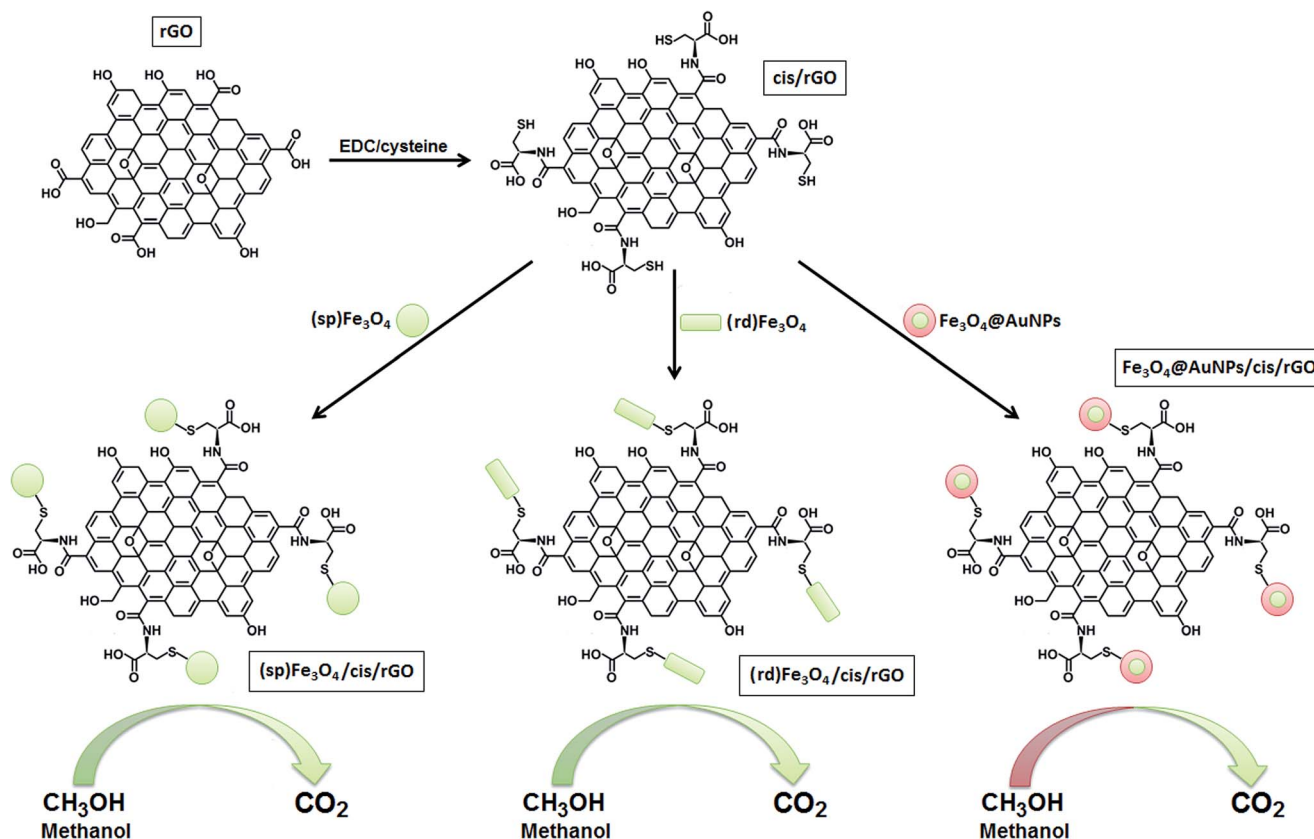
2.5. Preparation of (sp)Fe$_3$O$_4$/cys/rGO, (rd)Fe$_3$O$_4$/cys/rGO and Fe$_3$O$_4$@AuNPs/cys/rGO nanocomposites

rGO was dissolved in ethanol at 2 mg mL^{-1}. The mixture was sonicated to form a homogeneous suspension. The prepared rGO suspension was treated with 0.2 M of EDC solution for 8 h to ensure the surface activation of residual carboxylated groups. EDC compound provides the most popular and versatile method for labeling or crosslinking to free carboxylic groups on rGO.[33,34] The EDC molecules are considered zero-length carboxyl-to-amine crosslinkers. EDC reacts with carboxylic acid groups to form an active intermediate product that is easily displaced by nucleophilic attack from primary amino groups in the reaction mixture. The primary amine forms an amide bond with the original carboxyl group, and an EDC by-product is released as a soluble derivative. Therefore we used EDC for activation of free

carboxylic acid groups of rGO.[12,35] Then 1.0 mM cysteine was mixed with the activated rGO suspension at a 1 : 1 volume ratio and kept stirring for 2 h (cys/rGO). After that, 1 mg mL^{-1} of (sp) Fe$_3$O$_4$ solution was mixed with the 0.1 mg mL^{-1} of cys/rGO solution at a 1 : 1 volume ratio. Finally, the mixture was sonicated to generate a homogeneous mixture [(sp)Fe$_3$O$_4$/cys/rGO]. In a typical experiment of self-assembly, the aqueous dispersion of (rd)Fe$_3$O$_4$ and Fe$_3$O$_4$@AuNPs (1 mg mL^{-1}) was mixed with the aqueous dispersion of cys/rGO (0.1 mg mL^{-1}) at a 1 : 1 volume ratio and sonicated for 15 min to form a homogeneous mixture [(sp)Fe$_3$O$_4$/cys/rGO, (rd)Fe$_3$O$_4$/cys/rGO and Fe$_3$O$_4$@AuNPs/cys/ rGO]. The mixture was then kept undisturbed under ambient condition for 12 h.

2.6. Procedure for the electrode preparation

Glassy carbon electrodes (GCE) were cleaned by polishing with fine wet emery paper. They were polished with 0.1 μm and 0.05 μm alumina slurries, respectively on microcloth pads. The electrodes were sonicated twice in ultra-pure water and then in 50 : 50 (v/v) IPA and MeCN solution. After washing with water, glassy carbon electrode was washed with MeCN to eliminate any physisorbed materials. Finally, 20 μL of composite suspensions was dropped onto the GCE and then evaporating the solvent under an infrared heat lamp.

Scheme 1 The procedure of fabrication of the nanocomposites for methanol oxidation.

2.7. Electrochemical measurements

Electrocatalytic oxidation of 0.5 mol L^{-1} methanol on (sp)Fe_3O_4/cys/rGO, (rd)Fe_3O_4/cys/rGO and Fe_3O_4@AuNPs/cys/rGO was investigated in 0.1 mol L^{-1} $HClO_4$ solution by cyclic voltammetry (CV) between −0.5 and +1.5 V. The potentials were measured with respect to the Ag/AgCl electrode as a reference electrode. The counter electrode was a Pt wire.

The schematic diagram of the preparation of the nanocomposites for methanol oxidation is shown in Scheme 1.

3. Results and discussion

3.1. Characterizations of nanocomposites

The morphologies of the (sp)Fe_3O_4/cys/rGO, (rd)Fe_3O_4/cys/rGO and Fe_3O_4@AuNPs/cys/rGO nanocomposites were investigated by using the JEOL 2100 HRTEM with an accelerating voltage of 200 keV. A drop of sample solution was deposited on a polymeric grid dried at room temperature under an argon gas stream. Fig. 1A shows the transparent, wrinkled and planar sheet like morphology of rGO. In Fig. 1B, the TEM image of the (sp)Fe_3O_4/cys/rGO shows that the sizes of the (sp)Fe_3O_4 are very similar with a mean diameter of 18 to 20 nm on a lighter shaded substrate corresponding to rGO sheet. Fig. 1C shows the size of the (rd)Fe_3O_4/cys/rGO around 7–10 nm on the lighter shaded rGO sheets. Fig. 1D is the last TEM image that is corresponded to Fe_3O_4@AuNPs/cys/rGO and shows that the bimetallic Fe_3O_4@AuNPs have been seen as dark dots with a mean diameter of 12 to 15 nm on rGO sheets. Fig. 1E represents the EDX data of Fe_3O_4@AuNPs/cys/rGO composite to analyze the materials and the structure of the nanocomposite.

SEM characterization is used to investigate the morphologies of the developed surfaces in present study. In Fig. 2A, shows the smooth surface of bare GC electrode. Fig. 2B–D show dense layers covered on the GC electrode, indicating that the successful binding of (sp)Fe_3O_4/cys/rGO, (rd)Fe_3O_4/cys/rGO and Fe_3O_4@AuNPs/cys/rGO composites, respectively.

Fig. 3 shows the XPS spectrum of the nanocomposites, C, N, S, Fe of (sp)Fe_3O_4 (Fig. 3A), Fe of (rd)Fe_3O_4 (Fig. 3B) and Fe_3O_4@AuNPs (Fig. 3C) peaks are prominent, showing that (sp)Fe_3O_4, (rd)Fe_3O_4 and Fe_3O_4@AuNPs have been functionalized on the L-cysteine functionalized reduced graphene oxide sheets. The C_{1s} core-level spectra of the nanocomposites were curve-fitted in Fig. 3. The peaks at 283.4 eV, 284.3 eV and 286.4 eV are assigned to CH and CN and CONH, respectively.[11] The peak located at 397.4 eV in the N_{1s} narrow region XPS spectrum is corresponded to C–N groups in the covalent attachment of the carboxyl group of the reduced graphene oxide with the amino group of the cysteine.[12] S_{2p} region was curve-fitted with two components by a doublet ($2p^{1/2}$ and $2p^{3/2}$), owing to the spin–orbit coupling. The peak at 162.1 eV indicates that the sulfur atom in the nanocomposite was grafted with the nanoparticles. The peak at 163.2 eV can be assigned to free mercapto group in unreacted cysteine. Fig. 3A shows the Fe_{2p} region that characterized by doublet $2p^{1/2}$ and $2p^{3/2}$ signals that appear at 721.2 and 718.8 eV, respectively, corresponding the presence of Fe_3O_4 on (sp)Fe_3O_4/cys/rGO. The peak signals at 720.3 and 718.1 eV in Fig. 3B are corresponded to Fe $2p^{1/2}$ and $2p^{3/2}$, respectively, indicating the functionalization of (rd)Fe_3O_4. Fig. 3C shows the peaks at 720.6 and 718.3 eV of Fe_{2p} and peaks at 82.7 and 87.5 eV of Au_{4f} narrow region spectra of the Fe_3O_4@AuNPs/cys/rGO composite, respectively.[12]
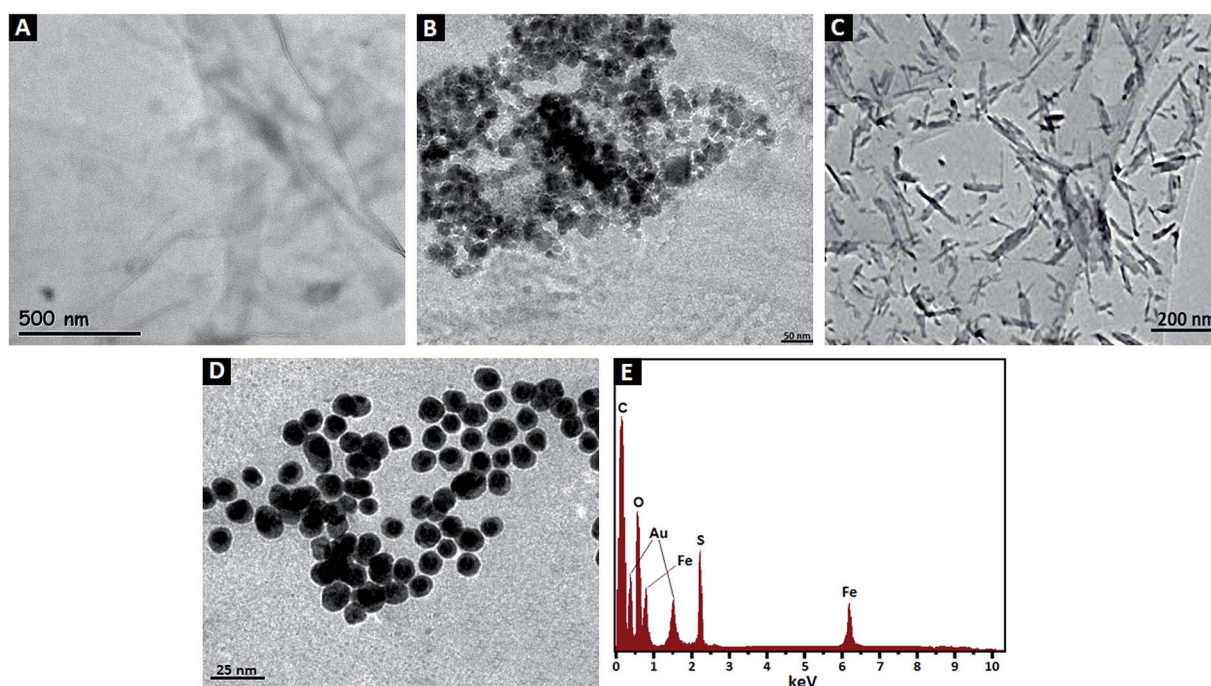

Fig. 1 TEM image of (A) rGO, (B) (sp)Fe_3O_4/cys/rGO, (C) (rd)Fe_3O_4/cys/rGO (D) Fe_3O_4@AuNPs/cys/rGO and (E) EDX data of Fe_3O_4@AuNPs/cys/rGO.
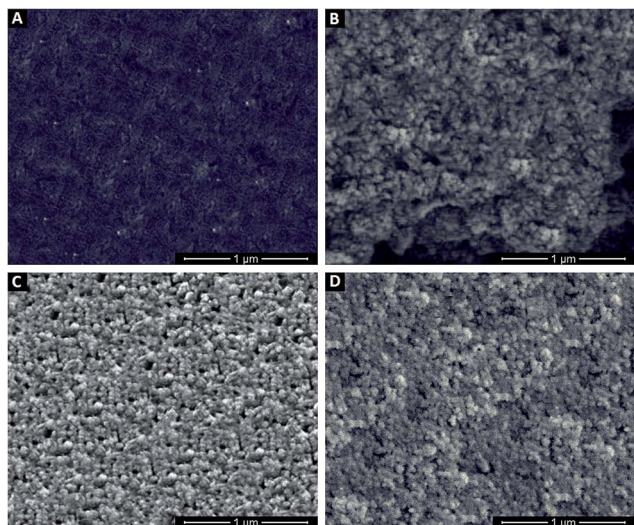
Fig. 2 SEM image of (A) bare GCE, (B) (sp)Fe_3O_4/cys/rGO/GCE, (C) (rd) Fe_3O_4/cys/rGO/GCE and (D) Fe_3O_4@AuNPs/cys/rGO/GCE.

The successful synthesis of the (sp)Fe_3O_4/cys/rGO, (rd)Fe_3O_4/cys/rGO and Fe_3O_4@AuNPs/cys/rGO composites were also confirmed by XRD patterns in Fig. 4. The XRD pattern of (sp)Fe_3O_4/cys/rGO composite is shown in Fig. 4A. The intense and narrow peaks at $2\theta = 34.16°$ and $42.23°$ refers to the (002) and (004) planes of rGO sheets, respectively.[36] The characteristic peaks of (sp)Fe_3O_4 also have been observed. The peaks at $2\theta = 30.08°$, $35.16°$, $38.24°$, $56.83°$ and $62.57°$ are corresponded to the (220), (311), (400), (511) and (440) planes of Fe, respectively. Fig. 4B shows the XRD pattern of (rd)Fe_3O_4/cys/rGO

composite. The intense and narrow peaks at $2\theta = 33.24°$ and $41.83°$ refers to the (002) and (004) planes of rGO sheets, respectively.[36] The peaks at $2\theta = 32.68°$, $37.12°$, $46.19°$, $54.61°$ and $61.83°$ are corresponded to the (220), (311), (400), (511) and (440) planes of Fe_3O_4, respectively. The XRD pattern of Fe_3O_4@AuNPs/cys/rGO composite is shown in Fig. 4C. The intense and narrow peaks at $2\theta = 22.46°$ and $36.52°$ refers to the (002) and (004) planes of rGO sheets, respectively. The peaks at $2\theta = 39.87°$ and $77.92°$ are corresponded to the (111) and (311) planes of Au, respectively. The characteristic peaks of Fe_3O_4@AuNPs also have been observed. The peaks at $2\theta = 45.06°$, $64.71°$ and $79.93°$ are corresponded to the Fe_3O_4(110)–Au(200), Fe_3O_4(200)–Au(220) and Fe_3O_4(211)–Au(222) planes, respectively.

3.2. Electrocatalytic activity for methanol oxidation

The electrocatalytic activities of (sp)Fe_3O_4/cys/rGO, (rd)Fe_3O_4/cys/rGO and Fe_3O_4@AuNPs/cys/rGO modified GCE were investigated by CV at 100 mV s^{-1} in a 0.1 mol L^{-1} HClO$_4$ solution. Fig. 5A shows the voltammograms of L-cysteine functionalized rGO, (sp)Fe_3O_4 and (sp)Fe_3O_4/cys/rGO, respectively. The peak current of 0.5 mol L^{-1} methanol on (sp)Fe_3O_4/cys/rGO modified GCE increases slowly at lower potentials and then quickly increases at potentials higher than 500 mV. The current density is directly proportional to the amount of methanol oxidized at the electrode. The observed current density on (sp)Fe_3O_4/cys/rGO modified GCE is much higher than (sp)Fe_3O_4 and cys/rGO modified GC electrodes. Fig. 5B shows the voltammograms of L-cysteine functionalized rGO, (rd)Fe_3O_4 and (rd)Fe_3O_4/cys/rGO, respectively and Fig. 5C shows the voltammograms of L-cysteine
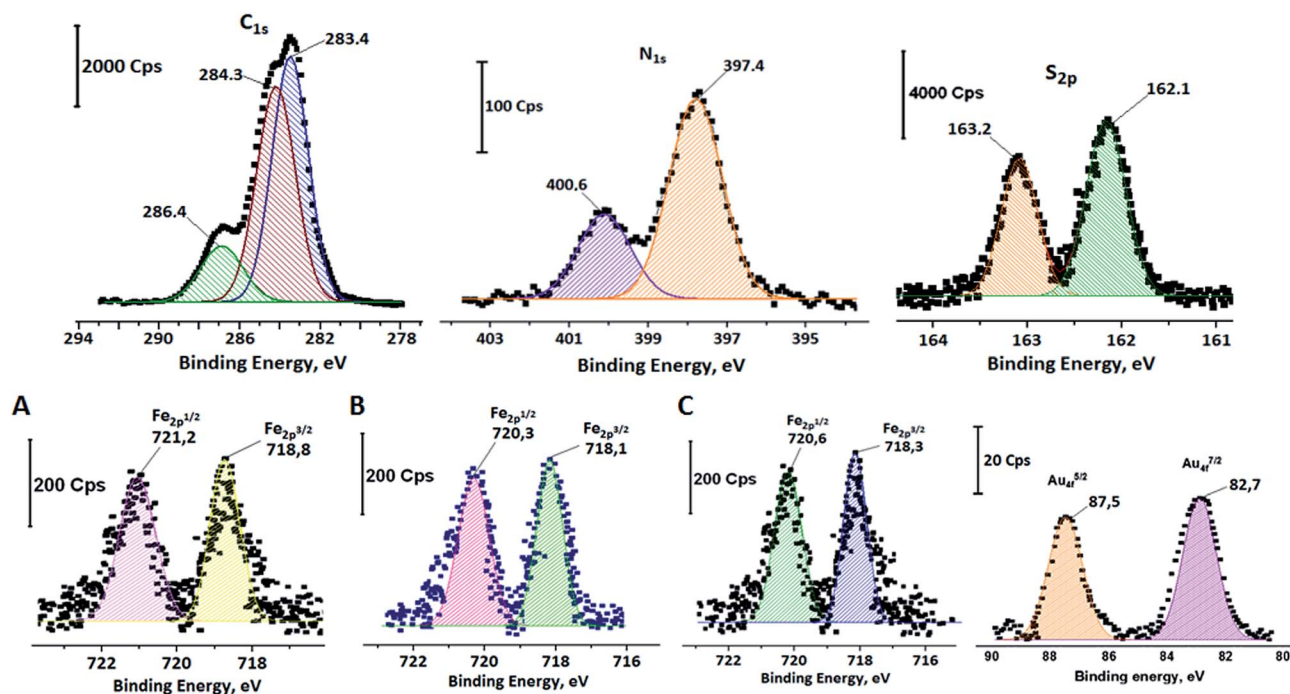

Fig. 3 The narrow region XPS spectra of (A) Fe_{2p} of (sp)Fe_3O_4/cys/rGO, (B) Fe_{2p} of (rd)Fe_3O_4/cys/rGO and (C) Fe_{2p} and Au_{4f} of Fe_3O_4@AuNPs/cys/rGO and C_{1s}, N_{1s} and S_{2p} of rGO.
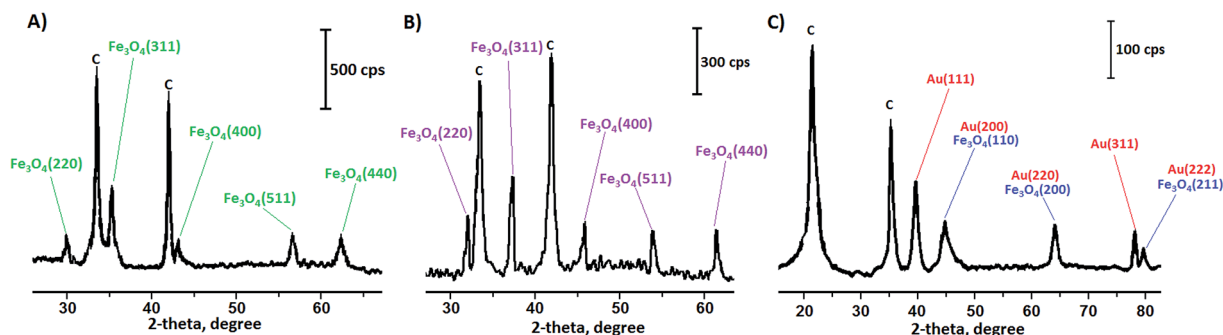
Fig. 4   XRD characterizations of (A) (sp)Fe$_3$O$_4$/cys/rGO, (B) (rd)Fe$_3$O$_4$/cys/rGO and (C) Fe$_3$O$_4$@AuNPs/cys/rGO.

functionalized rGO, Fe$_3$O$_4$@AuNPs and Fe$_3$O$_4$@AuNPs/cys/rGO, respectively. Fig. 5B and C are similar to Fig. 5A and shows that the current densities on (sp)Fe$_3$O$_4$/cys/rGO (Fig. 5B) and Fe$_3$O$_4$@AuNPs/cys/rGO (Fig. 5C) modified GC electrodes are much higher than (rd)Fe$_3$O$_4$ (Fig. 5B) and Fe$_3$O$_4$@AuNPs (Fig. 5C) and cys/rGO (both Fig. 5B and C) modified GC electrodes, which confirms that reduced graphene oxide-supported (sp)Fe$_3$O$_4$ (Fig. 5A), (rd)Fe$_3$O$_4$ (Fig. 5B) and Fe$_3$O$_4$@AuNPs (Fig. 5C) generate more complete oxidation of methanol to carbon dioxide.

The efficiencies of the (sp)Fe$_3$O$_4$/cys/rGO, (rd)Fe$_3$O$_4$/cys/rGO and Fe$_3$O$_4$@AuNPs/cys/rGO on methanol oxidation were compared with regard to oxidation potential and current densities in Table 1. As shown in Table 1, the oxidation peak potential of methanol for Fe$_3$O$_4$@AuNPs/cys/rGO was 554 mV, compared with an oxidation potential of 559 mV for (sp)Fe$_3$O$_4$/cys/rGO and an oxidation potential of 562 mV for (rd)Fe$_3$O$_4$/cys/

rGO. This observation shows that the Fe$_3$O$_4$@AuNPs/cys/rGO catalyst can significantly decrease the barrier to methanol oxidation and perform better than the other reduced graphene oxide-supported catalysts in Fig. 5D. As given in Fig. 6, for all reduced graphene oxide based electrocatalysts, the forward oxidation current (I) is proportional to the square root of the scan rate, suggesting that the oxidation behavior of methanol at all electrodes is controlled by diffusion processes. The slope for Fe$_3$O$_4$@AuNPs/cys/rGO electrocatalyst is larger than those for the other electrocatalysts, indicative of a faster diffusion process of methanol on the surface of Fe$_3$O$_4$@AuNPs/cys/rGO electrocatalyst.

In the literature, several catalysts were prepared for the fuel cell application. For example, Pt–Pd electrocatalysts supported on carbon microspheres (CMSs) were used for methanol oxidation in alkaline media.[37] Pt/CMS and Pd/CMS electrodes showed an activity of 11.4 mA cm^{-2} and 2.5 mA cm^{-2},
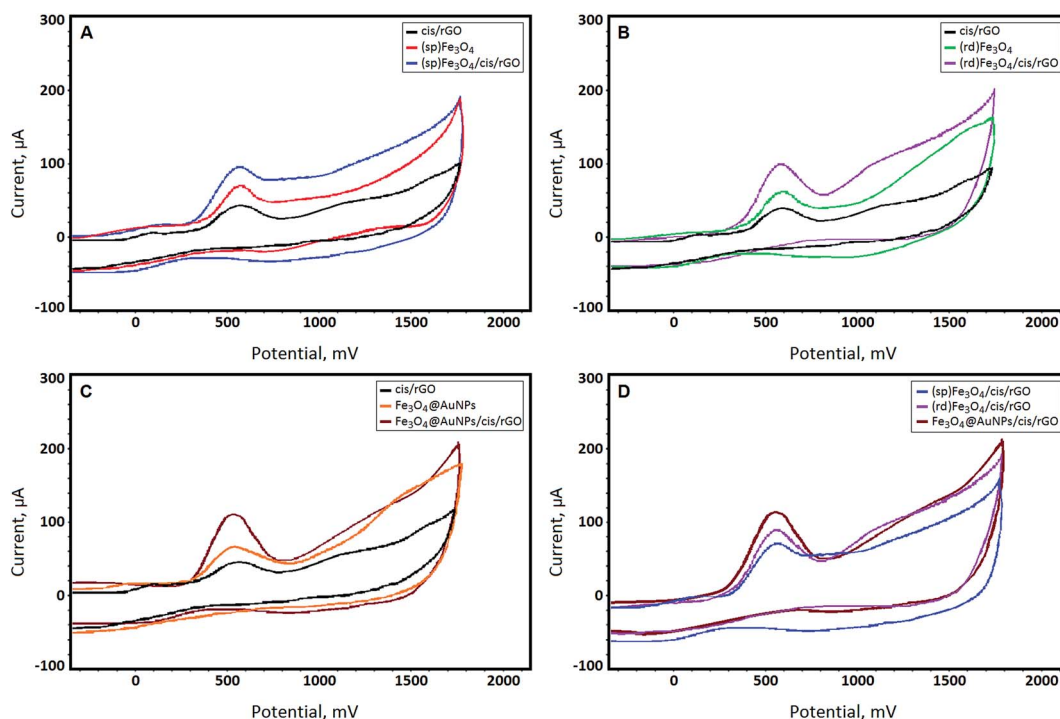

Fig. 5   The electrocatalytic activities of (A) cys/rGO, (sp)Fe$_3$O$_4$ and (sp)Fe$_3$O$_4$/cys/rGO, (B) cys/rGO, (rd)Fe$_3$O$_4$ and (rd)Fe$_3$O$_4$/cys/rGO, (C) cys/rGO, Fe$_3$O$_4$@AuNPs and Fe$_3$O$_4$@AuNPs/cys/rGO and (D) (sp)Fe$_3$O$_4$/cys/rGO, (rd)Fe$_3$O$_4$/cys/rGO and Fe$_3$O$_4$@AuNPs/cys/rGO.

Table 1 Comparison of electrocatalytic activity of methanol oxidation on bare GCE, rGO, (sp)Fe_3O_4/cys/rGO, (rd)Fe_3O_4/cys/rGO and Fe_3O_4@AuNPs/cys/rGO (scan rate: 100 mV s^{-1})

GC electrode	Peak current density (mA cm^{-2})	E (mV)
(sp)Fe_3O_4/cys/rGO	4.91 ± 0.1	559
(rd)Fe_3O_4/cys/rGO	6.23 ± 0.3	562
Fe_3O_4@AuNPs/cys/rGO	14.67 ± 0.2	554
rGO	0.64 ± 0.4	567
GCE	—	—
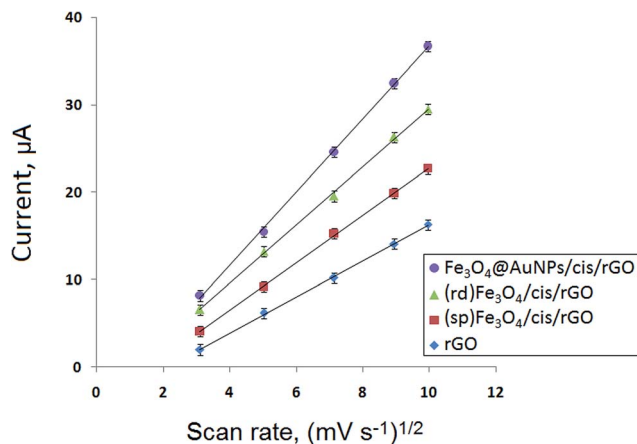
Fig. 6 The relationship of I vs. the square root of scan rate on reduced graphene oxide supported core–shell nanoparticle modified GCE.

respectively. Another study is pure Pt and nitrogen containing carbon nanotubes as platinum catalyst (Pt/N-CNT) showed an activity of 0.167 mA cm^{-2} and an activity of 13.3 mA cm^{-2}, respectively.[38] Recently, the Pt–Pd alloy porous films comprised of nanodendrites showed enhanced electrocatalytic activities toward the electrooxidation of methanol in acidic solution.[39] So we can say that the anodic current density of Fe_3O_4@AuNPs/cys/rGO catalyst is found to be higher than those of the mentioned electrodes, which indicate that the developed Fe_3O_4@AuNPs/
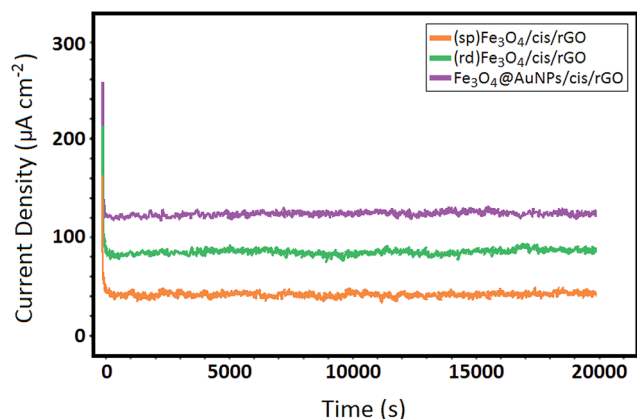
Fig. 7 Chronoamperometry results of (sp)Fe_3O_4/cys/rGO, (rd)Fe_3O_4/cys/rGO and Fe_3O_4@AuNPs/cys/rGO catalysts obtained in 0.5 M KOH and 1.0 M CH_3OH at 0.6 V.

cys/rGO catalyst have excellent catalytic activity on methanol electrooxidation.

The chronoamperometry measurements were performed to test the long-term stabilities of the as-prepared catalysts at 0.6 V in 0.5 M KOH and 1.0 M CH_3OH in Fig. 7. After the methanol oxidation reaction starts, it was found that Fe_3O_4@AuNPs/cys/rGO showed the highest oxidation current density at 20 000 s, which is 1.87 and 2.54 times as high as that observed on (rd)Fe_3O_4/cys/rGO and (sp)Fe_3O_4/cys/rGO, respectively. This indicates that Fe_3O_4@AuNPs/cys/rGO is more stable for methanol electro-oxidation than (rd)Fe_3O_4/cys/rGO and (sp)Fe_3O_4/cys/rGO, respectively.

4. Conclusion

Magnetic spherical iron oxide nanoparticles, rod iron oxide nanoparticles and iron@gold nanoparticles involved L-cysteine functionalized reduced graphene oxide nanohybrids were successfully synthesized and characterized. The results show that (sp)Fe_3O_4, (rd)Fe_3O_4 and Fe_3O_4@AuNPs were highly dispersed on the reduced graphene oxide nanosheets can more effectively enhance electrocatalytic activity of (sp)Fe_3O_4, (rd)Fe_3O_4 and Fe_3O_4@AuNPs for the oxidation of methanol into CO_2. Notably, the peak potential of methanol oxidation at Fe_3O_4@AuNPs/cys/rGO modified GCE is lower than (sp)Fe_3O_4/cys/rGO and (rd)Fe_3O_4/cys/rGO, respectively. Thus, it can be said that Fe_3O_4@AuNPs/cys/rGO show better electrocatalytic performance.

Acknowledgements

References

1 V. K. Gupta, M. L. Yola, N. Atar, Z. Üstündağ and A. O. Solak, *J. Mol. Liq.*, 2014, **191**, 172–176.

2 T. H. Thi Vu, T. T. Thi Tran, H. N. Thi Le, L. T. Tran, P. H. Thi Nguyen and N. Essayem, *J. Power Sources*, 2014, **276**, 340–346.

3 K. Ahn, M. Kim, K. Kim, H. Ju, I. Oh and J. Kim, *J. Power Sources*, 2015, **276**, 309–319.

4 J. Zhu, G. He and P. K. Shen, *J. Power Sources*, 2014, **275**, 279–283.

5 H. Wu, Y. Cao, Z. Li, G. He and Z. Jiang, *J. Power Sources*, 2014, **273**, 544–553.

6 W. Xu, S. Zhu, Z. Li, Z. Cui and X. Yang, *J. Power Sources*, 2014, **274**, 1034–1042.

7 Y. Ma, H. Li, H. Wang, X. Mao, V. Linkov, S. Ji, O. U. Gcilitshana and R. Wang, *J. Power Sources*, 2014, **268**, 498–507.

8 J. Huang, J. Zang, Y. Zhao, L. Dong and Y. Wang, *Mater. Lett.*, 2014, **137**, 335–338.

9 Y. Huang, H. Huang, Q. Gao, C. Gan, Y. Liu and Y. Fang, *Electrochim. Acta*, 2014, **149**, 34–41.

10 Y. Fang, X. Yang, L. Wang and Y. Liu, *J. Power Sources*, 2014, **267**, 33–38.

11 M. L. Yola, N. Atar and T. Eren, *Sens. Actuators, B*, 2014, **198**, 70–76.

12 M. L. Yola, T. Eren and N. Atar, *Biosens. Bioelectron.*, 2014, **60**, 277–285.

13 V. K. Gupta, M. L. Yola, T. Eren, F. Kartal, M. O. Çağlayan and N. Atar, *J. Mol. Liq.*, 2014, **190**, 133–138.

14 V. K. Gupta, N. Atar, M. L. Yola, Z. Üstündağ and L. Uzun, *Water Res.*, 2014, **48**, 210–217.

15 V. K. Gupta, N. Atar, M. L. Yola, M. Eryilmaz, H. Torul, U. Tamer, T. H. Boyaci and Z. Üstündağ, *J. Colloid Interface Sci.*, 2013, **406**, 231–237.

16 M. L. Yola, T. Eren and N. Atar, *Chem. Eng. J.*, 2014, **250**, 288–294.

17 H. Karimi-Maleh, A. L. Sanati, V. K. Gupta, M. Yoosefian, M. Asif and A. Bahari, *Sens. Actuators, B*, 2014, **204**, 647–654.

18 A. Pahlavan, H. Karimi-Maleh, F. Karimi, M. A. Amiri, Z. Khoshnama, M. R. Shahmiri and M. Keyvanfard, *Mater. Sci. Eng., C*, 2014, **45**, 210–215.

19 A. Baghizadeh, H. Karimi-Maleh, Z. Khoshnama, A. Hassankhani and M. Abbasghorbani, *Food Anal. Methods*, 2014, **8**, 549–557.

20 M. Najafi, M. A. Khalilzadeh and H. Karimi-Maleh, *Food Chem.*, 2014, **158**, 125–131.

21 M. L. Yola, T. Eren, N. Atar and S. Wang, *Chem. Eng. J.*, 2014, **242**, 333–340.

22 B. J. Sanghavi, S. M. Mobin, P. Mathur, G. K. Lahiri and A. K. Srivastava, *Biosens. Bioelectron.*, 2013, **39**, 124–132.

23 M. Baghayeri, H. Veisi, H. Veisi, B. Maleki, H. Karimi-Maleh and H. Beitollahi, *RSC Adv.*, 2014, **4**, 49595–49604.

24 B. J. Sanghavi, W. Varhue, J. L. Chávez, C. F. Chou and N. S. Swami, *Anal. Chem.*, 2014, **86**, 4120–4125.

25 B. J. Sanghavi, G. Hirsch, S. P. Karna and A. K. Srivastava, *Anal. Chim. Acta*, 2012, **735**, 37–45.

26 B. J. Sanghavi and A. K. Srivastava, *Analyst*, 2013, **138**, 1395–1404.

27 H. Karimi-Maleh, M. Moazampour, V. K. Gupta and A. L. Sanati, *Sens. Actuators, B*, 2014, **199**, 47–53.

28 M. L. Yola, V. K. Gupta, T. Eren, A. E. Şen and N. Atar, *Electrochim. Acta*, 2014, **120**, 204–211.

29 V. K. Gupta, M. L. Yola, M. S. Qureshi, A. O. Solak, N. Atar and Z. Üstündağ, *Sens. Actuators, B*, 2013, **188**, 1201–1211.

30 L. L. Tan, W. J. Ong, S. P. Chai and A. R. Mohamed, *Appl. Catal., B*, 2015, **166–167**, 251–259.

31 C. Zhai, M. Zhu, D. Bin, F. Ren, C. Wang, P. Yang and Y. Du, *J. Power Sources*, 2015, **275**, 483–488.

32 I. Martínez-Mera, M. E. Espinosa-Pesqueira, R. Pérez-Hernández and J. Arenas-Alatorre, *Mater. Lett.*, 2007, **61**, 4447–4451.

33 R. M. D. Soares, G. S. Maia, P. Rayas-Duarte and V. Soldi, *Food Hydrocolloids*, 2009, **23**, 181–187.

34 R. Barbucci, G. Giani, S. Fedi, S. Bottari and M. Casolaro, *Acta Biomater.*, 2012, **8**, 4244–4252.

35 M. L. Yola, T. Eren and N. Atar, *Sens. Actuators, B*, 2015, **210**, 149–157.

36 P. Bradder, S. K. Ling, S. Wang and S. Liu, *J. Chem. Eng. Data*, 2011, **56**, 138–141.

37 C. Xu, L. Cheng, P. Shen and Y. Liu, *Electrochem. Commun.*, 2007, **9**, 997–1001.

38 T. Maiyalagan, B. Viswanathan and U. V. Varadaraju, *Electrochem. Commun.*, 2005, **7**, 905–912.

39 J. Liu, L. Cao, W. Huang and Z. Li, *J. Electroanal. Chem.*, 2012, **686**, 38–45.